The Astrophysical Journal Letters, 995:L43 (13pp), 2025 December 20 https://doi.org/10.3847/2041-8213/ae2603

A Compact Multiplanet System of Three Transiting Giant Planets around TIC 118798035

Rafael Brahm[1,2], Trifon Trifonov[3,4,5], Andrés Jordán[1,2], Thomas Henning[3], Néstor Espinoza[6], Felipe I. Rojas[7], Marcelo Tala Pinto[8], Matías I. Jones[9], Daniel Thorngren[10], Lorena Acuña[3], Jan Eberhardt[3], Yared Reinarz[3], Helem Salinas[1], Michaela Vítková[11,12], Juan I. Espinoza-Retamal[2,7,13], Gaspar Bakos[13], Attila Bódi[13], Gavin Boyle[14,15], Zoltán Csubry[13], Joel Hartman[13], Anthony Keyes[13], Vincent Suc[1,2,14], and Geert Jan Talens[16]
[1] Facultad de Ingeniería y Ciencias, Universidad Adolfo Ibáñez, Av. Diagonal las Torres 2640, Peñalolén, Santiago, Chile
[2] Millennium Institute for Astrophysics, Nuncio Monseñor Sotero Sanz 100, Of. 104, Providencia, Santiago, Chile
[3] Max-Planck-Institut für Astronomie, Königstuhl 17, D-69117 Heidelberg, Germany
[4] Department of Astronomy, Sofia University "St Kliment Ohridski," 5 James Bourchier Blvd., BG-1164 Sofia, Bulgaria
[5] Landessternwarte, Zentrum für Astronomie der Universität Heidelberg, Königstuhl 12, D-69117 Heidelberg, Germany
[6] Space Telescope Science Institute, 3700 San Martin Dr., Baltimore, MD 21218, USA
[7] Instituto de Astrofísica, Pontificia Universidad Católica de Chile, Av. Vicuña Mackenna 4860, 7820436 Macul, Santiago, Chile
[8] Department of Astronomy, McPherson Laboratory, The Ohio State University, 140 W. 18th Ave., Columbus, OH 43210, USA
[9] European Southern Observatory (ESO), Alonso de Córdova 3107, Vitacura, Casilla 19001, Santiago, Chile
[10] Department of Physics and Astronomy, Johns Hopkins University, Baltimore, MD 21210, USA
[11] Astronomical Institute of the Czech Academy of Sciences, Fričova 298, CZ-25165 Ondřejov, Czech Republic
[12] Department of Theoretical Physics and Astrophysics, Faculty of Science, Masaryk University, Kotlářská 2, CZ-61137 Brno, Czech Republic
[13] Department of Astrophysical Sciences, Princeton University, 4 Ivy Lane, Princeton, NJ 08544, USA
[14] El Sauce Observatory—Obstech, Coquimbo, Chile
[15] Cavendish Laboratory, J. J. Thomson Avenue, Cambridge, CB3 0HE, UK
[16] Denys Wilkinson Building, Department of Physics, University of Oxford, OX1 3RH, UK
Received 2025 October 21; revised 2025 November 24; accepted 2025 November 26; published 2025 December 11

Abstract

We report the discovery and characterization of three transiting giant planets in the TIC 118798035 system. The three planets were identified as transiting candidates from data of the TESS mission and confirmed with ground-based photometric transit observations along with radial velocity variations obtained with FEROS, HARPS, and ESPRESSO. The three planets present transit timing variations (TTVs). We performed an *N*-body orbital fitting to the TTVs and radial velocities, finding that TIC 118798035 b is a warm low-density Neptune with a mass of $0.0250 \pm 0.0023\ M_J$, a radius of $0.655 \pm 0.018\ R_J$, and an orbital period of 11.507 days; TIC 118798035 c is a warm Saturn with a mass of $0.403 \pm 0.024\ M_J$, a radius of $0.973 \pm 0.023\ R_J$, and an orbital period of 22.564 days; and TIC 118798035 d is a warm Jupiter with a mass of $0.773 \pm 0.052\ M_J$, a radius of $0.923 \pm 0.044\ R_J$, and an orbital period of 48.925 days. The bulk metallicities of the three planets do not fully follow the mass–metallicity correlation found for the giant planets of the solar system, which hints at a somewhat different formation history for the planets of the TIC 118798035 system.

Unified Astronomy Thesaurus concepts: Exoplanet astronomy (486); Extrasolar gaseous giant planets (509); Transit timing variation method (1710); Radial velocity (1332); Transits (1711)

1. Introduction

Our solar system consists of a G-type dwarf star surrounded by eight planets in a coplanar configuration. Four of these eight planets are termed giant planets whose radii are larger than $3.8\ R_\oplus$ having extended primordial gaseous atmospheres. Thanks to different in situ measurements, it has been possible to conclude that these planets are enriched in metals compared to our Sun (B. Militzer et al. 2019; M. Podolak et al. 2019; S. Howard et al. 2023) and that their metallicity increases as the planet mass decreases. These observations are consistent with the core accretion theory of giant planet formation (J. B. Pollack et al. 1996).

In the past few decades, we have significantly improved our knowledge of the general structures and architectures of exoplanetary systems that contain giant planets (J. N. Winn & D. C. Fabrycky 2015; R. I. Dawson & J. A. Johnson 2018). A significant number of giant planets have been found orbiting in extreme proximity to their parent stars (hot Jupiters, $a < 0.1$ au). Hot Jupiters are preferentially found with no nearby planet companions (B. J. Hord et al. 2021), which has been attributed to high-eccentricity migration mechanisms for the formation of this population (e.g., C. Petrovich 2015). Warm Jupiters are gas giant planets orbiting beyond 0.1 au but inside the water snow line. This population of giant planets has been found to have a significantly larger fraction of companions than hot Jupiters (C. Huang et al. 2016), indicating that an important number of warm Jupiters experienced a quiescent disk-driven migration. This is also consistent with some warm Jupiters found in multiple systems close to orbital mean-motion resonances (MMRs; e.g., T. Trifonov et al. 2017, 2021; V. Bozhilov et al. 2023; J. Eberhardt et al. 2025; M. Vítková et al. 2025) and with the recently observed preponderance of warm Jupiters in single-star systems having low stellar obliquities (M. Rice et al. 2022; J. I. Espinoza-Retamal et al. 2025).

Transiting warm Jupiters are key objects for investigating the interior structure of giant exoplanets. These planets are not

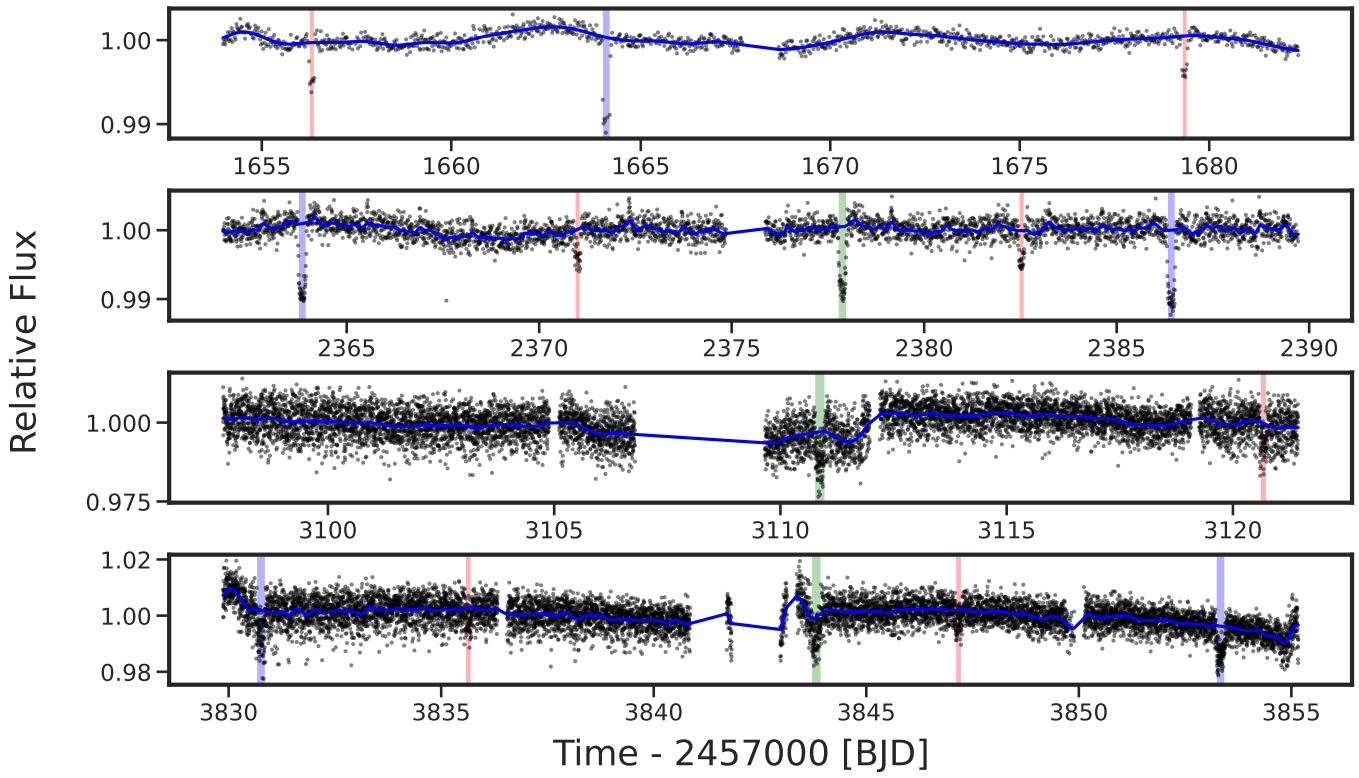

Figure 1. TESS light curves of TIC 118798035 from sectors 13, 39, 66, and 93, from top to bottom. Regions around transits of candidates b, c, and d are marked in red, blue, and green, respectively. We also plot the model for the out-of-transit variations computed with the Gaussian process described in Section 3.3.2.

subject to the mechanism that inflates the radii of hot Jupiters; therefore, standard interior models of planet structure can be used to infer their bulk metallicities (D. P. Thorngren et al. 2016; L. Acuña et al. 2024; Y. Chachan et al. 2025).

In some cases, multiple transiting warm gas giants have been found in the same system (e.g., D. C. Fabrycky et al. 2012; R. I. Dawson et al. 2021; T. Trifonov et al. 2023; D. E. Shaw et al. 2025). Nevertheless, planetary systems with more than two transiting giant planets are extremely scarce. These systems, while infrequent, are particularly interesting, because they allow us to investigate if the properties observed in our solar system giants are also present in other environments.

In this work, we present the discovery and characterization of an extrasolar system composed of a G-type dwarf star (TIC 118798035) orbited by three transiting warm giant planets ($R_P > 5\,R_\oplus$) in a compact configuration that was made in the context of the Warm gIaNts with tEss collaboration (WINE; R. Brahm et al. 2019; A. Jordán et al. 2020).

2. Observations

2.1. TESS

TIC 118798035 was monitored by the TESS mission (G. R. Ricker et al. 2015) in sectors 13, 39, 66, and 93 with cadences of 1800, 600, 200, and 200 s, respectively. For sectors 13 and 39, we retrieved the SPOC light curves of TIC 118798035 from MAST. For sectors 66 and 93, we generated the light curves using the `tesseract` pipeline.[17] These light curves were generated from the TESS full-frame images (TESS Team 2022). These four light curves contain transits of three different planet candidates (b, c, and d) with transit depths that are deep enough to be detected by the eye. TIC 118798035 b and TIC 118798035 c were reported as transiting candidates using a machine learning algorithm applied to all TESS-SPOC light curves of the primary TESS mission (H. Salinas et al. 2025). TIC 118798035 b has a transit depth of ≈5000 ppm and is present in all four TESS sectors. Candidate c has a depth of ≈9000 ppm and is present in sectors 13, 39, and 93. Candidate d is reported for the first time in the present study and has transits in sectors 39, 66, and 93 and a depth of ≈9000 ppm. The rough orbital periods of the two inner candidates are 11.507 and 22.564 days, respectively. However, some initial Keplerian fits to these light curves indicated the presence of significant transit timing variations (TTVs). In the case of TIC 118798035 d, since each TESS sector is separated by ∼2 yr and there is only one transit per sector, there were several possible orbital periods for this candidate. The longest possible orbital period for TIC 118798035 d was 733.00 days, and the shortest one was 38.58 days. The TESS light curves used in this study are presented in Figure 1.

The field around TIC 118798035 is moderately crowded, with several faint sources present. According to the Gaia DR3 catalog (Gaia Collaboration et al. 2023), there are 14 sources within a radius of 30″. The magnitude differences of these sources with respect to TIC 118798035 range from 5.3 to 9.1 mag in G. The SPOC light curves report a dilution factor (`CROWDSAP`) of 0.94 and 0.92 for sectors 13 and 39, respectively. We do not directly estimate the dilution factors for the light curves generated with `tesseract` for sectors 66 and 93, but we compute them through the analysis presented in Section 3.3.2.

[17] https://github.com/astrofelipe/tesseract.

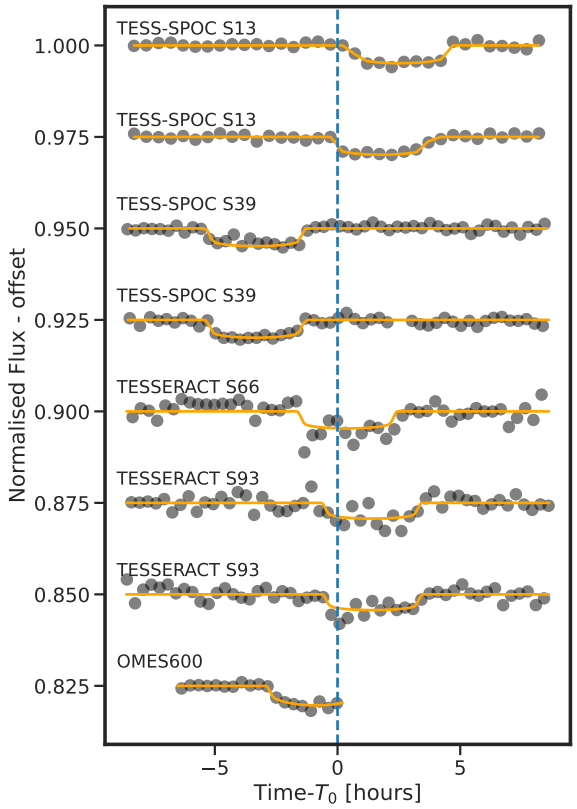

Figure 2. TESS and ground-based transits of TIC 118798035 b centered on the transit time predicted from a linear ephemeris. The transit model generated by `juliet` is also plotted for each transit.

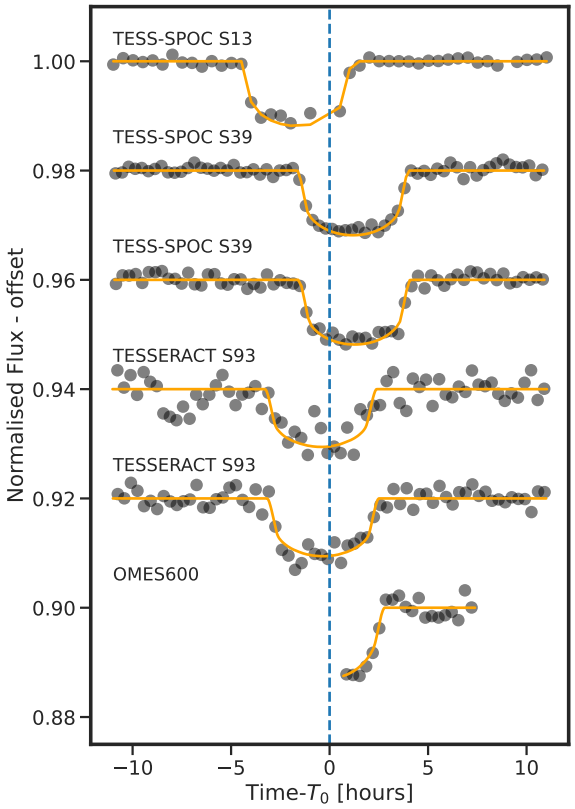

Figure 3. Same as Figure 2 but for TIC 118798035 c.

2.2. Ground-based Follow-up Observations

Given that the pixel scale of TESS is relatively large (20″), seeing-limited ground-based observations are required to confirm that the transit signals occur on the target star and not in close, fainter neighboring stars.

2.2.1. Observatoire Moana

Observatoire Moana is a network of small-aperture (0.5 and 0.6 m) robotic telescopes with two stations in El Sauce Observatory in Chile, one station in Siding Spring Observatory in Australia, one station in Spain, and two stations in the USA. We used the 0.6 m telescope at El Sauce (OMES600) to monitor one partial transit of TIC 118798035 b and one partial transit of TIC 118798035 c. We observed TIC 118798035 c on 2025 August 10 and TIC 118798035 b on 2025 August 16. In both cases, we used the Sloan *r*' filter and exposure times of 29 s. The data were processed with a dedicated and automated pipeline (R. Brahm et al. 2023; T. Trifonov et al. 2023). The OMES600 light curves are presented in Figures 2 and 3.

2.2.2. HATPI

HATPI[18] is a photometric instrument installed at Las Campanas Observatory (LCO) of the Carnegie Institution for Science. HATPI consists of a mosaic array of 64 identical lenses and cameras installed in a single mount, imaging the entire visible sky from LCO at 30 and 45 s cadence and 20″ pixel scale (G. Bakos et al. 2025, in preparation). We retrieved the HATPI light curve of TIC 118798035 through the HATPI data portal. These observations extend from 2024 February 27 to 2024 November 4 and were taken during HATPI's "shakedown operations" period.

2.3. High-resolution Spectroscopy

High-resolution spectroscopy is required to measure precision radial velocities (RVs) on the target star to identify periodic signals that can be attributed to the transiting candidates. These observations are fundamental in confirming the planetary nature of the transiting candidates. We used three different spectrographs to monitor the radial velocity variations of TIC 118798035. The RV values are presented in Table 1. These RVs have significant variations with amplitudes consistent with those produced by gas giant planets.

2.3.1. FEROS

TIC 118798035 was observed between 2024 July and 2025 September with the FEROS spectrograph (A. Kaufer et al. 1999) installed on the MPG 2.2 m telescope at the ESO La Silla Observatory. We obtained 27 spectra using exposure times of 1200 s. The observations were performed using the simultaneous calibration technique, with the second fiber illuminated by a ThAr lamp (A. Baranne et al. 1996), to trace instrumental drifts of the wavelength solution. FEROS data were processed with the automated `ceres` pipeline (R. Brahm et al. 2017a) to obtain precision RVs and bisector span measurements using the cross-correlation technique. We used the G2 binary mask as a template. We also computed the full width at half-maximum (FWHM) of the cross-correlation peak and the S-index that traces the stellar activity.

[18] https://hatpi.org

Table 1
RV and Activity Indices of TIC 118798035

BJD	RV (m s^{-1})	Bisector Span	FWHM	S-index	Instrument
2460516.66457690	13,617.1 ± 9.8	−6.0 ± 13.0	10,276.9 ± 13.0	−0.1811 ± 0.0191	FEROS
2460518.68752548	13,617.3 ± 11.0	24.0 ± 15.0	10,185.7 ± 15.0	0.2499 ± 0.0230	FEROS
2460534.63568115	13,726.7 ± 9.5	−5.0 ± 13.0	10,172.0 ± 13.0	0.2315 ± 0.0154	FEROS
2460536.57691066	13,696.6 ± 9.5	−9.0 ± 13.0	10,194.3 ± 13.0	0.2106 ± 0.0167	FEROS
2460537.56606724	13,711.8 ± 9.8	47.0 ± 13.0	10,354.1 ± 13.0	0.2163 ± 0.0177	FEROS
2460544.63757318	13,665.9 ± 13.1	−149.0 ± 16.0	10,309.1 ± 16.0	0.3405 ± 0.0340	FEROS
2460545.52587118	13,743.9 ± 12.4	24.0 ± 16.0	10,144.2 ± 16.0	0.1747 ± 0.0287	FEROS
2460546.56269445	13,649.8 ± 11.7	−1.0 ± 15.0	10,114.8 ± 15.0	0.1928 ± 0.0228	FEROS
2460547.51458969	13,699.3 ± 10.0	−45.0 ± 13.0	10,259.3 ± 13.0	0.1933 ± 0.0180	FEROS
2460582.56663757	13,751.2 ± 10.8	−13.0 ± 14.0	10,489.6 ± 14.0	0.3175 ± 0.0298	FEROS
2460584.63506224	13,669.7 ± 14.8	147.0 ± 18.0	10,312.7 ± 18.0	−0.0655 ± 0.0577	FEROS
2460589.59159943	13,718.5 ± 3.2	−34.1 ± 5.0	7652.8 ± 5.0	−0.015 ± 0.009	ESPRESSO
2460595.53553033	13,720.6 ± 5.4	−35.1 ± 6.0	7653.8 ± 6.0	−0.136 ± 0.014	ESPRESSO
2460605.53406674	13,665.7 ± 3.1	−73.7 ± 14.0	7702.4 ± 14.0	−0.839 ± 0.050	ESPRESSO
2460605.54883009	−10.0 ± 6.2	−36.0 ± 16.0	8446.4 ± 16.0	−1.5276 ± 0.0930	HARPS
2460610.55675713	−58.0 ± 4.1	−9.0 ± 11.0	8537.3 ± 11.0	−0.7456 ± 0.0466	HARPS
2460622.52120867	13,684.4 ± 14.3	−44.0 ± 17.0	10,537.8 ± 17.0	0.1895 ± 0.0407	FEROS
2460625.51130979	13,665.5 ± 10.3	52.0 ± 13.0	10,685.5 ± 13.0	0.2383 ± 0.0420	FEROS
2460741.87221931	21.8 ± 9.4	−14.0 ± 23.0	8600.8 ± 23.0	−3.6925 ± 0.2544	HARPS
2460745.84740885	−4.5 ± 2.3	−3.0 ± 7.0	8486.4 ± 7.0	0.0034 ± 0.0097	HARPS
2460735.85841482	13,750.1 ± 2.7	−43.1 ± 8.0	7643.1 ± 8.0	−0.3460 ± 0.020	ESPRESSO
2460738.80407461	13,704.0 ± 7.1	−12.7 ± 10.0	7700.6 ± 10.0	−0.358 ± 0.027	ESPRESSO
2460740.88443271	13,725.2 ± 4.4	−63.5 ± 5.0	7649.4 ± 5.0	−0.021 ± 0.009	ESPRESSO
2460743.84103942	13,678.7 ± 2.7	−42.9 ± 6.0	7623.0 ± 6.0	−0.061 ± 0.011	ESPRESSO
2460762.87223892	16.8 ± 9.5	12.0 ± 12.0	8551.8 ± 12.0	−0.0571 ± 0.0215	HARPS
2460763.89050326	1.0 ± 5.7	−6.0 ± 7.0	8499.0 ± 7.0	−0.0148 ± 0.0096	HARPS
2460775.88615376	85.4 ± 4.9	−30.0 ± 15.0	8483.7 ± 15.0	−0.4836 ± 0.0311	HARPS
2460790.90241155	−1.2 ± 1.6	17.0 ± 4.0	8480.7 ± 4.0	0.1162 ± 0.0075	HARPS
2460805.91564241	24.1 ± 3.9	10.0 ± 12.0	8474.1 ± 12.0	0.0412 ± 0.0080	HARPS
2460808.68981745	13,823.0 ± 13.8	41.0 ± 17.0	10,687.5 ± 17.0	0.4568 ± 0.0448	FEROS
2460819.81270876	36.7 ± 4.9	−13.0 ± 6.0	8508.7 ± 6.0	0.0569 ± 0.0097	HARPS
2460832.81446173	13,650.4 ± 9.2	19.0 ± 12.0	10,145.5 ± 12.0	0.1240 ± 0.0145	FEROS
2460833.90964164	19.4 ± 3.3	5.0 ± 11.0	8521.9 ± 11.0	−0.3220 ± 0.0218	HARPS
2460860.69465978	−38.5 ± 2.0	19.0 ± 6.0	8485.1 ± 6.0	0.0415 ± 0.0090	HARPS
2460868.68595354	44.2 ± 3.2	20.0 ± 10.0	84,503.0 ± 10.0	−0.0605 ± 0.0171	HARPS
2460872.67188090	50.7 ± 1.9	3.0 ± 5.0	8486.6 ± 5.0	0.0686 ± 0.0084	HARPS
2460875.75508209	13,706.3 ± 10.6	−57.0 ± 14.0	10,150.9 ± 14.0	0.2098 ± 0.0219	FEROS
2460900.63233013	13,538.4 ± 10.6	−37.0 ± 14.0	10,224.8 ± 14.0	0.1580 ± 0.0211	FEROS
2460911.61214084	13,657.7 ± 10.2	−17.0 ± 13.0	10,451.7 ± 13.0	0.3306 ± 0.0211	FEROS
2460912.60567926	49.5 ± 2.0	13.0 ± 6.0	8530.9 ± 6.0	0.0421 ± 0.0103	HARPS
2460913.59478035	13,764.6 ± 9.4	−34.0 ± 13.0	10,220.5 ± 13.0	0.2519 ± 0.0166	FEROS
2460927.66625271	13,727.6 ± 12.2	5.0 ± 15.0	10,237.7 ± 15.0	0.3896 ± 0.0389	FEROS
2460928.58258090	13,752.4 ± 12.5	−50.0 ± 15.0	10,451.5 ± 15.0	0.1957 ± 0.0269	FEROS
2460928.63713579	59.6 ± 2.5	3.0 ± 7.0	8532.0 ± 7.0	−0.0232 ± 0.0141	HARPS
2460929.61823672	13,674.3 ± 13.1	11.0 ± 16.0	10,334.0 ± 16.0	0.3500 ± 0.0274	FEROS
2460930.49609218	13,714.8 ± 8.2	42.0 ± 11.0	10,270.0 ± 11.0	0.2717 ± 0.0131	FEROS
2460938.65897170	13,812.9 ± 15.0	−106.0 ± 18.0	10,038.6 ± 18.0	0.2688 ± 0.0720	FEROS
2460940.58919492	13,741.9 ± 15.3	−95.0 ± 18.0	10,568.6 ± 18.0	0.0732 ± 0.0421	FEROS
2460941.61598775	13,726.8 ± 13.7	32.0 ± 17.0	10,076.6 ± 17.0	0.3249 ± 0.0451	FEROS
2460943.58286111	13,708.2 ± 14.8	−62.0 ± 18.0	10,164.3 ± 18.0	0.3884 ± 0.0470	FEROS

2.3.2. HARPS

We used the HARPS spectrograph (F. Pepe et al. 2002) installed at the ESO 3.6 m telescope at the ESO La Silla Observatory to monitor TIC 118798035 between 2024 October and 2025 September. Sixteen observations were obtained with exposure times of 1800 s. HARPS data were reduced with the dedicated HARPS data reduction software, and RVs were calculated with `serval` (M. Zechmeister et al. 2018), which uses a template-matching algorithm. We also independently obtained the bisector span measurements and FWHM and S-index values.

2.3.3. ESPRESSO

We also used the ESPRESSO spectrograph (F. Pepe et al. 2021), installed at the Very Large Telescope at the ESO Paranal Observatory, to monitor TIC 118798035 between 2024 October and 2025 March. We obtained seven spectra using exposure times of 600 s. ESPRESSO data were processed with the Data Reduction Software (DRS) version 3.3.0, and we used the RVs computed by the DRS. The DRS also delivers the measurement of the bisector span and FWHM. We obtained the stellar activity S-index from the ESPRESSO DAS Pipeline (version 1.3.8).

Table 2
Stellar Properties[a] of TIC 118798035

Parameter	Description	Value	Reference
R.A.	R.A. (J2015.5)	$18^h14^m54^s.77$	Gaia DR3[b]
decl.	decl. (J2015.5)	$-54^d26^m02^s.6$	Gaia DR3
$pm^{R.A.}$	Proper motion in R.A. (mas yr^{-1})	19.86 ± 0.05	Gaia DR3
$pm^{decl.}$	Proper motion in decl. (mas yr^{-1})	6.45 ± 0.05	Gaia DR3
π	Parallax (mas)	4.04 ± 0.02	Gaia DR3
d	Distance (pc)	242 ± 1.2	Gaia DR3
T	TESS magnitude (mag)	11.294 ± 0.006	TICv8[c]
B	B-band magnitude (mag)	12.7 ± 0.4	APASS[d]
V	V-band magnitude (mag)	11.99 ± 0.03	APASS
G	Gaia G-band magnitude (mag)	11.787 ± 0.002	Gaia DR3
G_{BP}	Gaia BP-band magnitude (mag)	12.190 ± 0.005	Gaia DR3
G_{RP}	Gaia RP-band magnitude (mag)	11.243 ± 0.003	Gaia DR3
J	2MASS J-band magnitude (mag)	10.59 ± 0.02	2MASS[e]
H	2MASS H-band magnitude (mag)	10.28 ± 0.02	2MASS
K_s	2MASS K_s-band magnitude (mag)	10.21 ±0.02	2MASS
$T_{\rm eff}$	Effective temperature (K)	5820 ± 80	This work
$\log g$	Surface gravity (cgs)	4.43 ± 0.02	This work
[Fe/H]	Metallicity (dex)	+0.20 ± 0.05	This work
$v \sin i_\star$	Projected rotational velocity (km s^{-1})	3.2 ± 0.5	This work
$M_\star$	Mass ($M_\odot$)	1.02 ± 0.03	This work
$R_\star$	Radius ($R_\odot$)	1.02 ± 0.02	This work
$L_\star$	Luminosity ($L_\odot$)	0.97 ± 0.02	This work
A_V	Visual extinction (mag)	0.18 ± 0.02	This work
Age	Age (Gyr)	$4.4^{+1.7}_{-1.6}$	This work
$\rho_\star$	Density (g cm^{-3})	$1.36^{+0.09}_{-0.08}$	This work

Notes.
[a] The errors in the stellar parameters presented in this study do not consider differences among different stellar evolutionary models (J. Tayar et al. 2022) and can be underestimated.
[b] Gaia Collaboration et al. (2023).
[c] K. G. Stassun et al. (2018, 2019). The TESS magnitude is shown only for reference and was not included in our stellar analysis.
[d] U. Munari et al. (2014).
[e] M. F. Skrutskie et al. (2006).

3. Analysis

3.1. Stellar Analysis

We adopted the procedure described in R. Brahm et al. (2019) to characterize the host star. This process is a two-step iterative methodology. The first step is to use the coadded HARPS spectrum to measure the atmospheric stellar parameters ($T_{\rm eff}$, $\log(g)$, [Fe/H], and $v \sin(i)$) using the `zaspe` package (R. Brahm et al. 2017b), which compares the high-resolution spectrum against a grid of synthetic models. The second step consists of a spectral energy distribution (SED) fit to public broadband photometry of the star using the PARSEC stellar evolution models (A. Bressan et al. 2012) and the Gaia DR3 (Gaia Collaboration et al. 2023) parallax. In this step, we use the spectroscopic derived $T_{\rm eff}$ as a prior, and we fix the metallicity of that obtained with `zaspe`. With this SED fit, we obtain a more precise measurement of the stellar $\log(g)$, which we held fixed in a new run of `zaspe`. The iteration continues until reaching convergence in the measured atmospheric parameters. The results of our stellar analysis are presented in Table 2. We find that TIC 118798035 is a metal-rich ([Fe/H] = +0.20 ± 0.05) G-type dwarf star not too different from our own Sun.

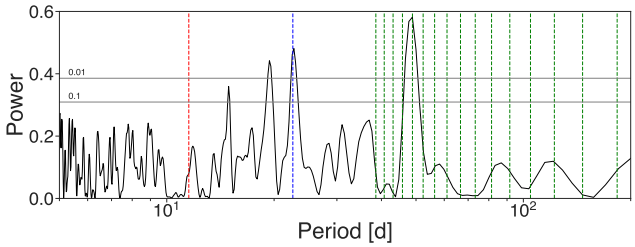

Figure 4. GLS periodogram generated from the FEROS, HARPS, and ESPRESSO RVs of TIC 118798035. The horizontal lines correspond to the 10% and 1% false-alarm probabilities. The red and blue dashed vertical lines mark the orbital periods of candidates b and c, respectively. The green dashed vertical lines mark the possible period aliases of TIC 118798035 d based on TESS photometry.

3.2. Radial Velocities

We computed the generalized Lomb–Scargle (GLS) periodogram after combining the RVs of FEROS, HARPS, and ESPRESSO in a single dataset. We take into account the errors of the RVs to generate the GLS. The periodogram is presented in Figure 4. It is possible to distinguish two significant peaks above 5 days. The peak with the second-highest power is consistent with the orbital period of TIC 118798035 c. There is no significant peak close to the orbital period of TIC 118798035 b, probably due to the relatively low mass of this smaller giant planet. The peak of highest significance on the periodogram is consistent with one of the possible orbital periods of TIC 118798035 d (48.8 days), which is strong evidence in favor of this period alias for the true period of this outer planet. We also computed the GLS periodograms for the bisector span, FWHM, and S-index measurements, which are shown in Figure 5. There are no significant peaks in these periodograms, supporting the view that the signals present in the RVs are of planetary origin and not produced by stellar activity or false-positive scenarios.

3.3. Light-curve Analysis

3.3.1. Transit of TIC 118798035 d in HATPI

The RV analysis presented in Section 3.2 allowed us to constrain the most probable orbital period for TIC 118798035 d to 48.87 days. We inspected the HATPI light curve and identified that during the night of 2024 July 10, an ingress-like feature is present in the data, whose timing is consistent with the 48.925 day orbital period. This event rules out all other possible period aliases and confirms that the orbital period of TIC 118798035 d is 48.925 days. The HATPI light curve for this night is presented in Figure 6.

We also used the full HATPI light curve to infer the rotational period of the star. We computed the GLS of the light curve and found a significant peak at $P_{\rm rot} = 16.4 \pm 1.6$ days. If we combine this value with the radius of the star derived from our stellar analysis, we obtain an equatorial rotational velocity

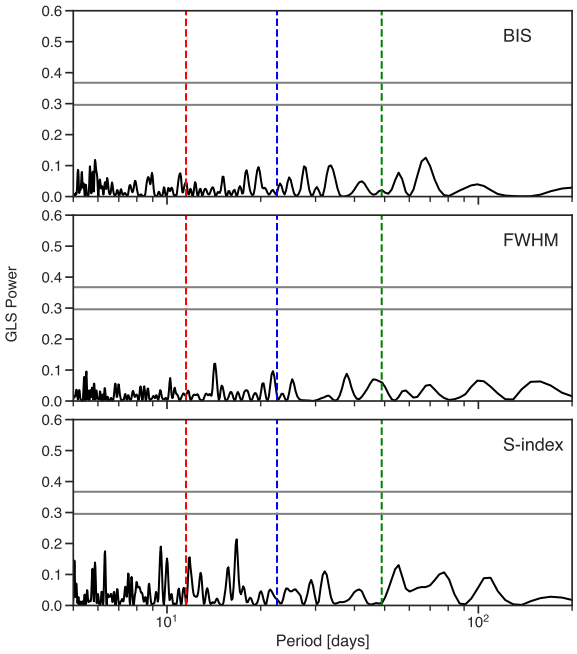

Figure 5. Same as in Figure 4 but for the bisector spans, FWHM, and S-index. Here the green dashed line corresponds to the orbital period of TIC 118798035 d constrained by the RVs and HATPI light curve.

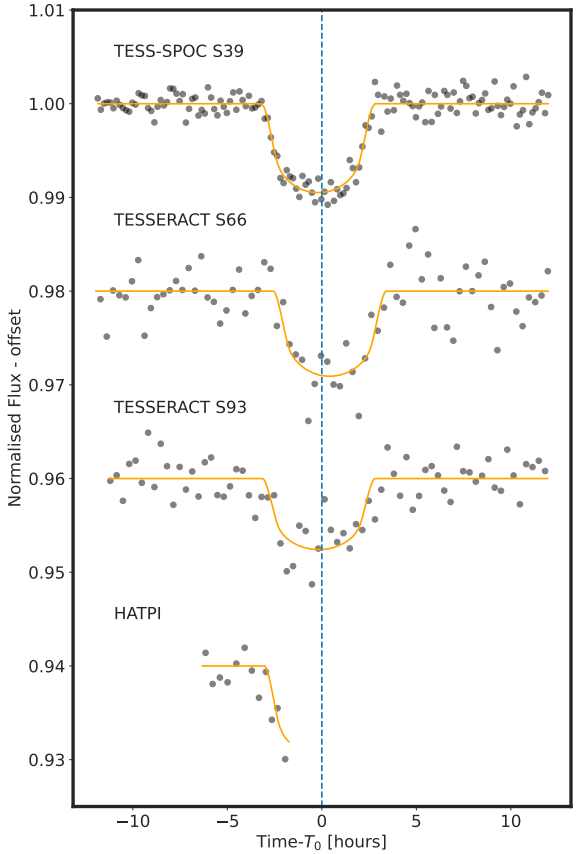

Figure 6. Same as Figure 2 but for TIC 118798035 d.

of $v_{\rm eq} = 3.1 \pm 0.3\,{\rm km\,s^{-1}}$. This value is fully consistent with the projected rotational velocity obtained with `zaspe`, which implies an inclination of the stellar rotation axis close to 90° with respect to the line of sight and a probable low stellar obliquity for the TIC 118798035 planetary system.

Table 3
Priors and Posteriors for the TTV Extraction with juliet for TIC 118798035 b

Parameter	Prior	Posterior
b	$\mathcal{U}$ (0.0,1.0)	$0.39^{+0.05}_{-0.07}$
$R_P/R_\star$	$\mathcal{U}$ (0.0,1.0)	$0.066^{+0.001}_{-0.001}$
$q_{1,\rm TESS}$	$\mathcal{U}$ (0.0,1.0)	$0.2^{+0.1}_{-0.1}$
$q_{2,\rm TESS}$	$\mathcal{U}$ (0.0,1.0)	$0.5^{+0.3}_{-0.3}$
$q_{1,\rm OMES600}$	$\mathcal{U}$ (0.0,1.0)	$0.7^{+0.2}_{-0.2}$
$\rho_\star$ (kg cm^{-3})	$\mathcal{N}$ (1360,100)	1390^{+100}_{-90}
$m_{\rm dilution,S66}$	$\mathcal{U}$ (0.5,1.0)	$0.96^{+0.03}_{-0.05}$
$m_{\rm dilution,S93}$	$\mathcal{U}$ (0.5,1.0)	$0.89^{+0.07}_{-0.08}$
$\sigma_{w,\rm S13}$ (ppm)	$\mathcal{J}$ (0.1,1000.0)	4^{+27}_{-3}
$\sigma_{w,\rm S39}$ (ppm)	$\mathcal{J}$ (0.1,1000.0)	70^{+240}_{-70}
$\sigma_{w,\rm S66}$ (ppm)	$\mathcal{J}$ (0.1,1000.0)	3880^{+30}_{-30}
$\sigma_{w,\rm S93}$ (ppm)	$\mathcal{J}$ (0.1,1000.0)	3520^{+30}_{-30}
$\sigma_{w,\rm OMES600}$ (ppm)	$\mathcal{J}$ (0.1,1000.0)	1300^{+200}_{-200}
$T_{\rm b,0}$ (BJD)	$\mathcal{N}$ (2458656.3,0.5)	$2458656.321^{+0.002}_{-0.002}$
$T_{\rm b,2}$ (BJD)	$\mathcal{N}$ (2458679.4,0.5)	$2458679.352^{+0.002}_{-0.002}$
$T_{\rm b,62}$ (BJD)	$\mathcal{N}$ (2459371.0,0.5)	$2459371.000^{+0.002}_{-0.002}$
$T_{\rm b,63}$ (BJD)	$\mathcal{N}$ (2459382.5,0.5)	$2459382.532^{+0.002}_{-0.002}$
$T_{\rm b,127}$ (BJD)	$\mathcal{N}$ (2460120.7,0.5)	$2460120.673^{+0.004}_{-0.004}$
$T_{\rm b,189}$ (BJD)	$\mathcal{N}$ (2460835.7,0.5)	$2460835.638^{+0.008}_{-0.007}$
$T_{\rm b,190}$ (BJD)	$\mathcal{N}$ (2460847.2,0.5)	$2460847.170^{+0.007}_{-0.006}$
$T_{\rm b,195}$ (BJD)	$\mathcal{N}$ (2460904.8,0.5)	$2460904.730^{+0.003}_{-0.003}$

3.3.2. Light-curve Modeling and TTV Extraction

We used the TESS light curves of the four sectors along with the OMES600 and HATPI light curves to model the transits of the three planets present in the TIC 118798035 system. We first masked out all the transits present in the TESS light curves and used the `juliet` package (N. Espinoza et al. 2019) to perform a fit to the out-of-transit flux in order to detrend these light curves. The light curve of each TESS sector was modeled with a different Gaussian process. In all cases, we used a Matern 3/2 kernel.

We then used the detrended TESS light curves and the ground-based light curves to model the transits of the TIC 118798035 system with `juliet`. We adopted the parameterization that allows the user to fit the times of each transit individually instead of fitting the orbital period and time of the first transit. We applied this parameterization given the presence of significant TTVs for the three planets. For this analysis, we assumed circular orbits for the three planets. For the TESS light curves, we used the quadratic limb-darkening law, while for the ground-based light curves, we used a linear one. We adopted the parameterization in which we fit for the stellar density instead of the normalized semimajor axis and used the value obtained in Section 3.1 as a prior. For sectors 66 and 93 of TESS, we allowed the dilution factor to vary between 0.5 and 1.0. Given that the SPOC light curves are already corrected by dilution from nearby sources, we fixed the dilution factor to 1. For the ground-based light curves, we assumed no flux contamination by neighbor stars and fixed the dilution factor to 1. We run different `juliet` fits for the different planets. The results of these three fits are presented in Tables 3, 4, and 5.

3.4. N-*body Orbital Fitting*

3.4.1. Methods and Parameterization

We performed a joint TTV and RV orbital analysis using the `Exo-Striker` fitting tool (T. Trifonov 2019), which

Table 4
Priors and Posteriors for the TTV Extraction with juliet for TIC 118798035 c

Parameter	Prior	Posterior
b	$\mathcal{U}$ (0.0,1.0)	$0.1^{+0.1}_{-0.1}$
$R_P/R_\star$	$\mathcal{U}$ (0.0,1.0)	$0.098^{+0.001}_{-0.001}$
$q_{1,\mathrm{TESS}}$	$\mathcal{U}$ (0.0,1.0)	$0.36^{+0.06}_{-0.07}$
$q_{2,\mathrm{TESS}}$	$\mathcal{U}$ (0.0,1.0)	$0.5^{+0.3}_{-0.3}$
$q_{1,\mathrm{OMES600}}$	$\mathcal{U}$ (0.0,1.0)	$0.8^{+0.1}_{-0.1}$
$\rho_\star$ (kg cm^{-3})	$\mathcal{N}$ (1360,100)	1350^{+50}_{-70}
$m_{\mathrm{dilution,S93}}$	$\mathcal{U}$ (0.5,1.0)	$0.89^{+0.04}_{-0.04}$
$\sigma_{w,\mathrm{S13}}$ (ppm)	$\mathcal{J}$ (0.1,1000.0)	3^{+39}_{-3}
$\sigma_{w,\mathrm{S39}}$ (ppm)	$\mathcal{J}$ (0.1,1000.0)	20^{+220}_{-20}
$\sigma_{w,\mathrm{S93}}$ (ppm)	$\mathcal{J}$ (0.1,1000.0)	3500^{+30}_{-30}
$\sigma_{w,\mathrm{OMES600}}$ (ppm)	$\mathcal{J}$ (0.1,1000.0)	3400^{+200}_{-200}
$T_{\mathrm{c,0}}$ (BJD)	$\mathcal{N}$ (2458664.1,0.5)	$2458664.092^{+0.001}_{-0.001}$
$T_{\mathrm{c,31}}$ (BJD)	$\mathcal{N}$ (2459363.9,0.5)	$2459363.847^{+0.001}_{-0.001}$
$T_{\mathrm{c,32}}$ (BJD)	$\mathcal{N}$ (2459386.4,0.5)	$2459386.419^{+0.001}_{-0.001}$
$T_{\mathrm{c,96}}$ (BJD)	$\mathcal{N}$ (2460830.8,0.5)	$2460830.760^{+0.005}_{-0.006}$
$T_{\mathrm{c,97}}$ (BJD)	$\mathcal{N}$ (2460853.3,0.5)	$2460853.334^{+0.003}_{-0.003}$
$T_{\mathrm{c,99}}$ (BJD)	$\mathcal{N}$ (2460898.5,0.5)	$2460898.484^{+0.002}_{-0.002}$

Table 5
Priors and Posteriors for the TTV Extraction with juliet for TIC 118798035 d

Parameter	Prior	Posterior
b	$\mathcal{U}$ (0.0,1.0)	$0.65^{+0.04}_{-0.04}$
$R_P/R_\star$	$\mathcal{U}$ (0.0,1.0)	$0.093^{+0.003}_{-0.003}$
$q_{1,\mathrm{TESS}}$	$\mathcal{U}$ (0.0,1.0)	$0.6^{+0.3}_{-0.3}$
$q_{2,\mathrm{TESS}}$	$\mathcal{U}$ (0.0,1.0)	$0.4^{+0.3}_{-0.3}$
$q_{1,\mathrm{HATPI}}$	$\mathcal{U}$ (0.0,1.0)	$0.7^{+0.2}_{-0.4}$
$\rho_\star$ (kg cm^{-3})	$\mathcal{N}$ (1360,100)	1340^{+100}_{-100}
$m_{\mathrm{dilution,S66}}$	$\mathcal{U}$ (0.5,1.0)	$0.95^{+0.03}_{-0.03}$
$m_{\mathrm{dilution,S93}}$	$\mathcal{U}$ (0.5,1.0)	$0.80^{+0.09}_{-0.06}$
$\sigma_{w,\mathrm{S39}}$ (ppm)	$\mathcal{J}$ (0.1,1000.0)	7^{+86}_{-7}
$\sigma_{w,\mathrm{S66}}$ (ppm)	$\mathcal{J}$ (0.1,1000.0)	3880^{+30}_{-30}
$\sigma_{w,\mathrm{S93}}$ (ppm)	$\mathcal{J}$ (0.1,1000.0)	3520^{+30}_{-30}
$\sigma_{w,\mathrm{HATPI}}$ (ppm)	$\mathcal{J}$ (0.1,1000.0)	11^{+203}_{-11}
$T_{\mathrm{d,0}}$ (BJD)	$\mathcal{N}$ (2459377.9,0.5)	$2459377.876^{+0.002}_{-0.002}$
$T_{\mathrm{d,15}}$ (BJD)	$\mathcal{N}$ (2460110.9,0.5)	$2460110.872^{+0.004}_{-0.004}$
$T_{\mathrm{d,23}}$ (BJD)	$\mathcal{N}$ (2460501.8,0.5)	$2460501.768^{+0.008}_{-0.009}$
$T_{\mathrm{d,30}}$ (BJD)	$\mathcal{N}$ (2460843.9,0.5)	$2460843.817^{+0.007}_{-0.006}$

incorporates an internally self-consistent RV *N*-body model, together with an *N*-body model for the TTVs based on the `ttvfast` tool. A similar approach has already been used in several of our WINE TTV exoplanet studies, for example, for the TOI-2202 system (T. Trifonov et al. 2021), the TOI-2525 system (T. Trifonov et al. 2023), and the TOI-4504 system (M. Vítková et al. 2025). We refer the reader to T. Trifonov et al. (2021) and M. Vítková et al. (2025) for further details on the numerical methods used for the TTV+RV modeling scheme.

Briefly, our scheme combines three sets of TTVs for each transiting planet (TIC 118798035 b, c, and d) and precise RV data from FEROS, HARPS, and ESPRESSO. The planetary parameterization is done in the Jacobi frame (M. Lee & S. Peale 2003) and includes the osculating planetary orbital periods $P_{\mathrm{b,c,d}}$; the parameters $h_{\mathrm{b,c,d}} = e_{\mathrm{b,c,d}} \sin \omega_{\mathrm{b,c,d}}$, $k_{\mathrm{b,c,d}} = e_{\mathrm{b,c,d}} \cos \omega_{\mathrm{b,c,d}}$; and the mean longitude angles $\lambda_{\mathrm{b,c,d}} = \omega_{\mathrm{b,c,d}} + M_{\mathrm{b,c,d}}$ (see X. Tan et al. 2013). From these combinations of parameters, $e_{\mathrm{b,c,d}}$ are the planetary eccentricities, $\omega_{\mathrm{b,c,d}}$ are the arguments of periastron, and $M_{\mathrm{b,c,d}}$, are the mean anomalies. The planetary dynamical masses in the *N*-body model were estimated by fitting the RV semiamplitudes $K_{\mathrm{b,c,d}}$. We allow the planetary inclinations $i_{\mathrm{b,c,d}}$ to vary within the derived posterior ranges obtained from the TTV extraction fit. However, we keep fixed at 0° the line of node angles $\Omega_{\mathrm{b,c,d}}$ needed to fully characterize the three-dimensional geometry of the orbits, since these are very difficult to constrain and remain undefined. Therefore, we assumed an edge-on yet mutually inclined system, which is the most likely configuration if we observe the three objects in transit (D. Ragozzine & M. J. Holman 2010; J. Brakensiek & D. Ragozzine 2016). The RVs were modeled with individual instrumental offsets and jitter terms, $\mathrm{RV_{off}}$ and $\mathrm{RV_{jitt}}$, for the FEROS, HARPS, and ESPRESSO datasets. The osculating orbital parameters are given for the reference epoch BJD = 2458656.3, selected to precede the first observed transit of TIC 118798035 b. The *N*-body model adopts the stellar mass estimate derived from our analysis (see Table 2), namely, $M_\star = 1.024 \pm 0.05\, M_\odot$. The integration time step of the *N*-body model was set to $dt = 0.1$ day, which is very small given the long temporal baseline of the observations but strictly necessary due to the short orbital period of the innermost planet, ensuring sufficient numerical accuracy with approximately 100 integration steps per completed orbit.

3.4.2. Best-fit Parameters and Posteriors

To explore the vast orbital parameter space of the three interacting warm giant planets, we performed a global parameter search using the `dynesty` nested sampler (NS; J. S. Speagle 2020), implemented within the `Exo-Striker` tool (see M. Vítková et al. 2025 for details). The prior ranges were informed by individual RV analyses, including GLS periodograms and prewhitening RV cascade fits with multi-Keplerian and *N*-body models, as well as by the TTV extraction parameters derived from the transit data. We adopted 100 live points per fitted parameter and employed the static NS configuration.

The NS posteriors were calculated primarily to identify the most likely regions of parameter space consistent with the data. Given the high computational cost of the full *N*-body modeling and the strong parameter degeneracies, a fully converged NS posterior characterization for TIC 118798035 would require a very large number of NS live points and an unfeasible number of CPU hours to complete the task. For similar computational constraints, we decided against performing a complete photodynamical analysis of the light curves and RVs, as it would demand excessive computational resources with minimal gain compared to the simpler yet accurate TTV+RV modeling scheme.

Instead, we identified the best $-\ln \mathcal{L}$ solution from the NS run and refined it using an iterative simplex optimization (J. A. Nelder & R. Mead 1965) to obtain the global best-fit parameters. The posterior probability distributions and the corresponding 1σ parameter uncertainties were subsequently derived with an affine-invariant ensemble Markov Chain Monte Carlo (MCMC) sampler (J. Goodman & J. Weare 2010), implemented through the `emcee` package (D. Foreman-Mackey et al. 2013).

3.4.3. Results

Our MCMC posterior results from the joint TTV+RV modeling of the TIC 118798035 system are summarized in Table 6, and the corresponding posterior probability

Table 6
Best-fit (Maximum-likelihood) Parameters and Median Values with 1σ Credible Intervals from the TTV+RV Model Posterior

Parameter	Best Fit (Max. *lnL*)	Median and 1σ
RV Offsets and Jitters		
RV $\mathrm{off}_{\mathrm{FEROS}}$ (m s^{-1})	13,684.6	$13{,}683.3^{+7.5}_{-5.6}$
RV $\mathrm{off}_{\mathrm{HARPS}}$ (m s^{-1})	30.7	$29.8^{+4.1}_{-5.7}$
RV $\mathrm{off}_{\mathrm{ESPR}}$ (m s^{-1})	13,684.3	$13{,}681.3^{+5.5}_{-4.5}$
RV $\mathrm{jitt}_{\mathrm{FEROS}}$ (m s^{-1})	34.3	$32.2^{+6.4}_{-4.0}$
RV $\mathrm{jitt}_{\mathrm{HARPS}}$ (m s^{-1})	19.0	$22.8^{+3.1}_{-3.7}$
RV $\mathrm{jitt}_{\mathrm{ESPR}}$ (m s^{-1})	9.1	$13.0^{+5.6}_{-2.8}$
Orbital Parameters		
K_b (m s^{-1})	2.26	$2.22^{+0.20}_{-0.18}$
P_b (days)	11.5076	$11.5075^{+0.0017}_{-0.0015}$
$e \sin \omega_b$	0.0497	$0.0517^{+0.0038}_{-0.0039}$
$e \cos \omega_b$	0.0494	$0.0464^{+0.0041}_{-0.0044}$
λ_b (deg)	83.9	$84.26^{+0.49}_{-0.49}$
i_b (deg)	89.9	$89.94^{+0.53}_{-0.44}$
K_c (m s^{-1})	28.9	$28.7^{+1.2}_{-1.7}$
P_c (days)	22.5635	$22.5644^{+0.0027}_{-0.0024}$
$e \sin \omega_c$	0.0049	$0.0068^{+0.0051}_{-0.0055}$
$e \cos \omega_c$	0.0313	$0.0268^{+0.0061}_{-0.0061}$
λ_c (deg)	322.1	$322.66^{+0.69}_{-0.73}$
i_c (deg)	90.3	$90.05^{+0.43}_{-0.52}$
K_d (m s^{-1})	40.8	$42.5^{+2.3}_{-2.6}$
P_d (days)	48.9273	$48.9244^{+0.0048}_{-0.0054}$
$e \sin \omega_d$	−0.055	$-0.0492^{+0.012}_{-0.012}$
$e \cos \omega_d$	0.0621	$0.0548^{+0.0088}_{-0.0097}$
λ_d (deg)	166.1	$167.0^{+1.2}_{-1.1}$
i_d (deg)	89.96	$89.93^{+0.53}_{-0.44}$
Derived Planetary and Orbital Quantities		
m_p(b) (M_J)	0.0250	$0.0250^{+0.0024}_{-0.0022}$
m_p(c) (M_J)	0.4007	$0.4033^{+0.0237}_{-0.0251}$
m_p(d) (M_J)	0.7297	$0.7728^{+0.0514}_{-0.0520}$
a_b (au)	0.0996	$0.1006^{+0.0016}_{-0.0017}$
a_c (au)	0.1560	$0.1575^{+0.0025}_{-0.0026}$
a_d (au)	0.2615	$0.2640^{+0.0042}_{-0.0044}$
R_b (R_J)	…	0.655 ± 0.018
R_c (R_J)	…	0.973 ± 0.023
R_d (R_J)	…	0.923 ± 0.044
$T_{eq,b}$ (K)	…	872 ± 8
$T_{eq,c}$ (K)	…	696 ± 7
$T_{eq,d}$ (K)	…	538 ± 5

Note. The orbital elements are valid for epoch BJD = 2458656.3.

distributions are shown in Figure A1. In Table 6, we report the posterior median values and their 1σ credible intervals derived from the combined TTV and RV data. Figures 7 and 8 present the resulting best-fit model from our joint *N*-body TTV+RV analysis, which provides an excellent representation of the observations and is therefore considered robust.

Overall, our analysis reveals that TIC 118798035 hosts a dynamically compact and well-aligned system of three warm giant planets with well-constrained orbital and physical parameters. The joint fit yields a system composed of three gravitationally interacting planets, designated as TIC 118798035 b, c, and d, with osculating orbital periods of $P_b = 11.5075^{+0.0017}_{-0.0015}$, $P_c = 22.5644^{+0.0027}_{-0.0024}$, and $P_d = 48.9244^{+0.0048}_{-0.0054}$ days, corresponding to semimajor axes of $a_b = 0.1006^{+0.0016}_{-0.0017}$, $a_c = 0.1575^{+0.0025}_{-0.0026}$, and $a_d = 0.2640^{+0.0042}_{-0.0044}$ au, respectively.

The orbital eccentricities are small but significantly different from circular, with $e_b = 0.0517^{+0.0038}_{-0.0039}$, $e_c = 0.0068^{+0.0051}_{-0.0055}$, and $e_d = 0.049^{+0.012}_{-0.012}$. Assuming nearly coplanar configurations with small mutual inclinations and accounting for the stellar mass and its uncertainty, we derive well-constrained dynamical planetary masses of $m_b = 0.0250^{+0.0024}_{-0.0022}$, $m_c = 0.403^{+0.024}_{-0.025}$, and $m_d = 0.773^{+0.051}_{-0.052}$ M_J, corresponding to a sub-Neptune, a Saturn-mass planet, and a Jupiter-mass planet, respectively.

The three planets are close to first-order commensurability with average period ratios of $P_c/P_b \approx 1.96$ and $P_d/P_c \approx 2.17$. However, a detailed *N*-body inspection of the orbital dynamics does not reveal any evidence of a low-order MMR between the warm giants.

We further performed a comprehensive *N*-body dynamical analysis of the MCMC posterior samples using the symplectic *N*-body integrator `SyMBA` (M. J. Duncan et al. 1998), following the same stability setup as applied in previous WINE TTV studies (see T. Trifonov et al. 2021, 2023; J. Eberhardt et al. 2025; M. Vítková et al. 2025). Long-term stability analysis shows that the system is dynamically stable over secular timescales. From 1000 randomly selected MCMC posterior samples integrated over 1 Myr, the TIC 118798035 planetary system remained stable and dynamically well separated in all cases. Interestingly, about half of the integrated configurations exhibit libration of the secular apsidal angle of planets TIC 118798035 c and d, defined as $\Delta\omega_{c-d} = \omega_c - \omega_d$. The libration occurs around 0° with an amplitude of about 70°, suggesting that the secular coupling between the outer Jovian planets dominates the long-term dynamical evolution of the system.

Figure 9 illustrates a representative dynamical evolution of the three-planet system for an extent of 1000 yr. The top panels of Figure 9, from left to right, show the evolution of the semimajor axes, the orbital eccentricities, and the inclinations, respectively. The bottom panels of Figure 9, from left to right, show the evolution of the period ratio between planets TIC 118798035 b and c, P_c/P_b; the period ratio between planets TIC 118798035 c and d, P_d/P_c; and the secular apsidal angle $\Delta\omega_{c-d}$, which clearly exhibits libration around 0°, consistent with a secular coupling.

The remaining stable configurations consistent with the TTV and RV data do not show any secular or resonant angle libration, indicating that the system may be chaotic but still long-term stable. It is plausible that the three planets were originally trapped in a Laplace 1:2:4 MMR resonance chain and subsequently escaped from this synchronization due to overstability effects (P. Goldreich & H. E. Schlichting 2014). In this scenario, convergent planetary migration with strongly damped eccentricities could only have led to a transient resonance capture at the 2:1/2:1 commensurability, followed by dynamical relaxation into the present near-resonant configuration.

3.5. Interior Modeling

To determine the bulk composition of the TIC 118798035 system planets, we use the interior structure models of D. Thorngren & J. J. Fortney (2019). These solve the equations of hydrostatic equilibrium, mass conservation, and an appropriate equation of state to determine the size of a given model planet. We used the S. L. Thompson (1990) equations of state for the heavy elements, which were set at a 50–50 mixture of rock and ice; for hydrogen and helium, we

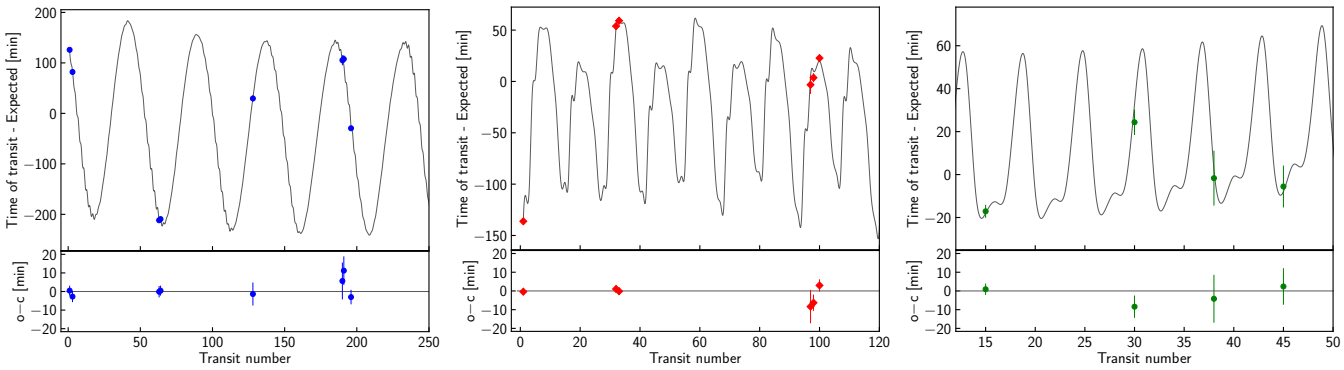

Figure 7. TTV time series and best-fit model of TIC 118798035 b, c, and d. The bottom panels show the TTV model residuals.

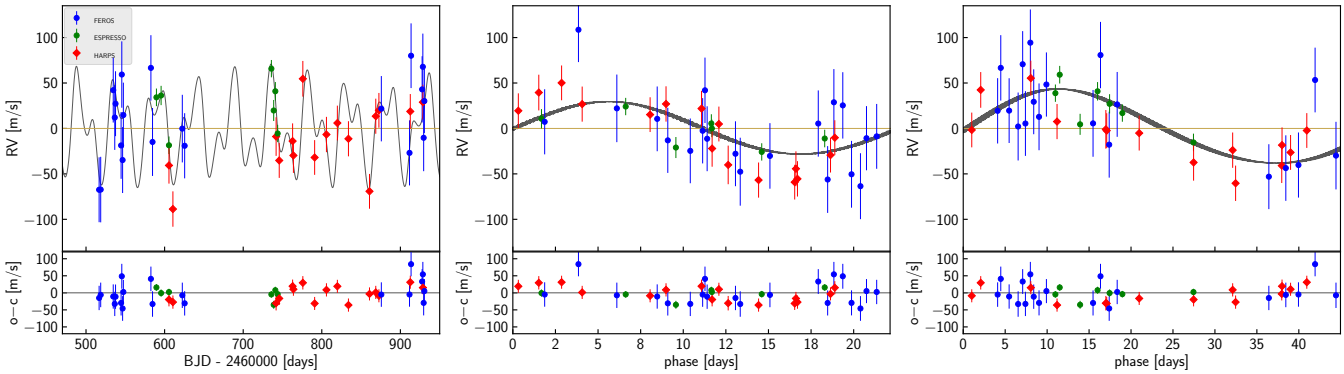

Figure 8. Same model as in Figure 7 but applied in the FEROS, HARPS, and ESPRESSO RV time series. The left panel shows the full model to the RVs. The middle panel shows the phased signal for TIC 118798035 c after removing the contribution of the other planets. The right panel shows the phased model signal TIC 118798035 d after removing the contribution of the other planets. The signal of TIC 118798035 b is too small and practically unconstrained; thus, is not shown. The bottom panels show the RV model residuals. The error bars include the jitter obtained from the analysis presented in Section 3.4.

used G. Chabrier & F. Debras (2021; who incorporate entropy results from B. Militzer & W. B. Hubbard 2013). To thermally evolve the planets, we use the atmosphere models of J. J. Fortney et al. (2007).

The models are fit to the observed mass, radius, instellation, and age using a Bayesian framework (D. Thorngren & J. J. Fortney 2019) to determine the bulk metallicity. The model parameters for c and d are the mass, metallicity, and age, with priors for mass and age set to the observed values with uncertainties, and the prior for metallicity is from the D. P. Thorngren et al. (2016) mass–metallicity relation (accounting for the wide population spread).

TIC 118798035 c and d are warm gas giants of fairly typical composition. For c, we obtain a bulk metallicity of $Z = 0.15 \pm 0.03$, which sets a limit on the atmospheric metallicity (D. Thorngren & J. J. Fortney 2019) of $<19.2 \times$ solar. Relative to the parent star, we have $Z_p/Z_* = 6.72^{+1.6}_{-1.5}$. Similarly, for planet d, we have $Z = 0.22 \pm 0.05$, an atmospheric metallicity limit of $<33.2 \times$ solar, and $Z_p/Z_* = 9.86^{+2.4}_{-2.6}$. Note that these uncertainties are largely driven by the shared stellar uncertainties. As such, the relative metallicity between c and d is better constrained than the absolute metallicity. For example, if the true stellar radius were 1σ above the observational mean, it would imply that both planets are larger and therefore have less metal, but the effect would be similar between planets. The modeling uncertainties associated with systematic errors of the equation of state are not taken into account in the error bars presented but would also be similar between planets (e.g., Y. Miguel et al. 2016; D. P. Thorngren et al. 2016; S. Howard et al. 2025). Another source of systematic uncertainty could be differences in the distribution of metals within the planet (e.g., sharply defined core, diffuse core, or fully mixed interior), but this will probably differ most between gas and ice giants (e.g., D. P. Thorngren et al. 2016; S. Bloot et al. 2023). A strong source of systematic uncertainty would be the trap of heat in a H/He-enriched core (J. Leconte & G. Chabrier 2012), but the lack of inflated warm giants tends to lean against that as a major effect. Lastly, the initial entropy can affect the radii of young super-Jupiters but not the older and lower-mass planets we consider in this Letter. In summary, even considering that systematic model uncertainties are not explicitly included in the error budget of the planet bulk metallicities, we can conclude that the result that planet d is more metal-rich than c is secure.

Although it is also in the warm giant regime, TIC 118798035 b has a much more ambiguous composition. As it is a sub-Neptune, we have adjusted our model accordingly, allowing the ice-to-rock ratio and the fraction of ice mixed into the envelope (versus an outer layer of the core) to vary as additional free parameters. The prior distributions for both additional parameters are set as uniform between 0 and 1. This covers scenarios in which the planet might be water-rich due to forming outside the ice line versus water-poor due to forming within it. For more massive planets, this is a small effect, but for sub-Neptunes, it is important.

In this case, for a water-poor model, the metallicity is $Z \approx 0.6$, whereas more water-rich models allow metallicities

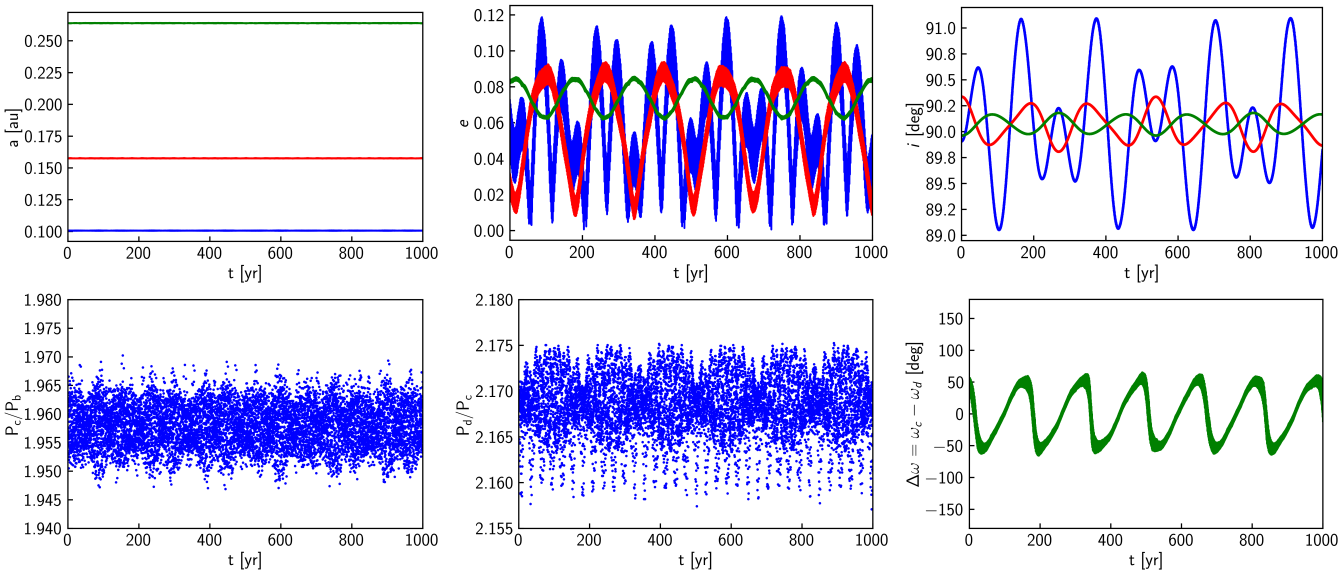

Figure 9. Orbital evolution of the TIC 118798035 system for an extent of 1000 yr for the best-fit (maximum $-lnL$) sample from the MCMC posteriors. Top panels, from left to right: evolution of the planetary semimajor axes, eccentricities, and inclinations, where TIC 118798035 b is shown with blue, TIC 118798035 c with red, and TIC 118798035 d with green. Bottom panels, from left to right: evolution of the period ratio between the inner pair P_c/P_b, the outer pair P_d/P_c, and the libration of the apsidal angle $\Delta\omega_{c-d}$ in aligned configuration around 0°.

exceeding $Z > 0.9$. As such, we cannot place a limit on the atmospheric metallicity. We can only set a lower limit on the bulk metallicity, $Z > 0.55$, and relative to the parent star, $Z_p/Z_* > 20$, but it could easily be much higher.

4. Discussion and Conclusions

In this work, we reported the discovery and characterization of an exoplanetary system consisting of three transiting warm giant planets orbiting the solar-type G dwarf star TIC 118798035 in a compact and nearly resonant configuration. TIC 118798035 b is an inflated Neptune with an orbital period of 11.507 days. TIC 118798035 c is warm Saturn with an orbital period of 22.564 days. Finally, TIC 118798035 d is a warm Jupiter with an orbital period of 48.925 days. The low mutual inclinations of these three planets, their nearly resonant configuration, and the low inferred stellar obliquity indicate that the planets probably experienced gentle disk migration from beyond the snow line (P. Goldreich & S. Tremaine 1979).

The TIC 118798035 system is one of the very few known systems that contains more than two giant ($R_P > 0.5\ R_J$) transiting planets (see Figure 10). For example, the Kepler-31 system (D. C. Fabrycky et al. 2012) presents three transiting giant planets, but all have radii similar to Neptune. The Kepler-51 system contains three planets with radii between Neptune and Jupiter, but all these planets fall in the rare category of superpuffs (K. Masuda et al. 2024). Another comparable system is V1298 Tau (T. J. David et al. 2019), which has four transiting planets larger than Neptune, but due to the young age of the star, the masses of these planets are mostly unconstrained (B. Finociety et al. 2023). TIC 118798035 stands out as the only system with three transiting giant planets with precise masses suitable for atmospheric studies.

Due to the detailed characterization of the planets of the TIC 118798035 system, we were able to model the interior structure of the planets and infer their bulk metallicities. Figure 11 shows the relative metal enrichment of these planets as a function of the planet mass, where we also indicate the values for three planets of the solar system (Neptune, Saturn, and Jupiter). The Neptune-mass planet in both systems seems to be significantly enhanced in metals compared to the gas giants. This is expected for core-dominated planets that did not enter into the runaway gas accretion stage. However, we can identify an important difference between the TIC 118798035 system and the solar system. The metallicities of TIC 118798035 c and d are comparable, and TIC 118798035 d could even have a higher fraction of heavy elements than TIC 118798035 c. This goes in the opposite direction of the mass–metallicity correlation seen in our solar system but can still be consistent within the error bars with the empirical mass–metallicity relation for warm giant planets found in Y. Chachan et al. (2025). The total inferred amount of heavy elements in Saturn and Jupiter is comparable ($\sim$20 $M_\oplus$), indicating a roughly similar history of envelope enrichment with planetesimals/pebbles throughout their evolution. For the TIC 118798035 system, we find that the total amount of heavy elements of TIC 118798035 d ($55 \pm 12\ M_\oplus$) is significantly larger than that of TIC 118798035 c ($18 \pm 4\ M_\oplus$), which is consistent with the empirical correlation found by D. P. Thorngren et al. (2016). This difference in the amount of solids accreted could be explained by differences in the migration distance covered by both planets (S. Shibata et al. 2020), where TIC 118798035 d formed significantly beyond the snow line and was able to accrete a large fraction of planetesimals and/or pebbles (C. Danti et al. 2023) during its viscous migration into the inner parts of the system. In this case, we would expect different atmospheric compositions for both exterior giants of the TIC 118798035 system. Another possibility is that similar superstellar bulk metallicities of both gas giants were produced by accretion of similar volatile-enriched gas due to the evaporation of icy pebbles that drifted from beyond the snow line (A. D. Schneider & B. Bitsch 2021). In this case, while accreting gas of similar composition inside the snow line, the difference in final masses for both planets could originate from a delayed runaway gas accretion of TIC 118798035 c compared to

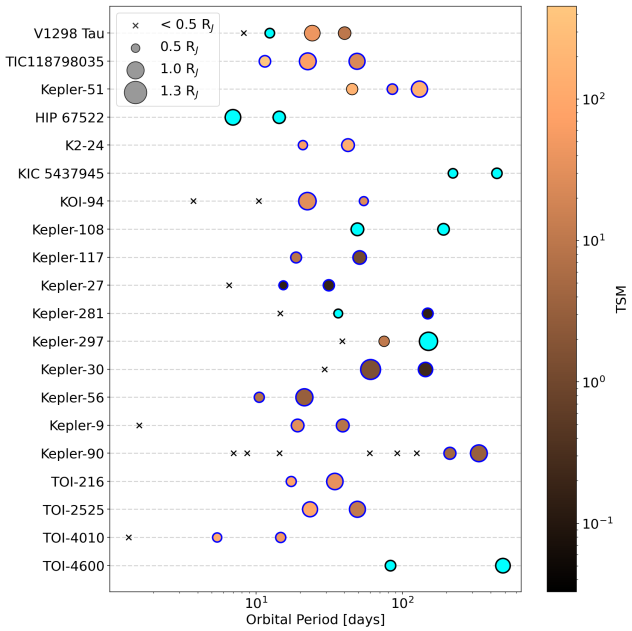

Figure 10. Systems containing two or more transiting planets with a radius larger than 0.5 R_J. The size of the circles scales up with the planet radius. Planets with masses measured with a precision better than 20% have blue borders. The circles are color-coded by transmission spectroscopy metric (TSM).

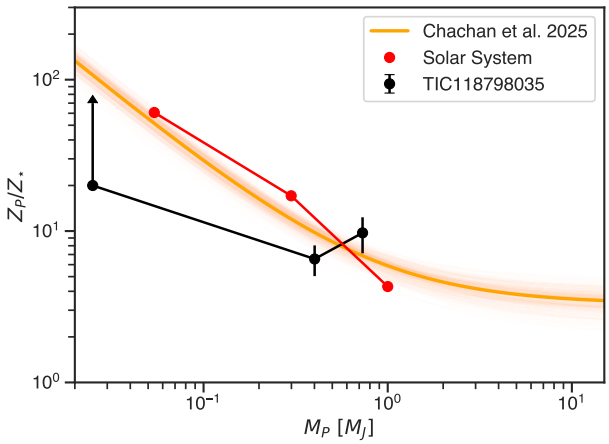

Figure 11. Relative planet bulk metallicities as a function of the planet mass for the TIC 118798035 system (black circles) and the solar system (Neptune, Uranus, Jupiter; red circles). We also show the empirical relation found by Y. Chachan et al. (2025).

TIC 118798035 d (C. Bergez-Casalou et al. 2023). In this scenario, we should expect similar atmospheric metallicities and C/O ratios for TIC 118798035 c and TIC 118798035 d, which could be tested in the future.

TIC 118798035 b is significantly larger than Neptune but has half of its mass and can therefore be categorized as a fluffy sub-Neptune-mass planet in the "Savanna" region (V. Bourrier et al. 2023). TIC 118798035 b is among the sub-Neptune-mass planets with the lowest bulk density. The mild insolation that it receives could be inflating the planet envelope, but given that this planet is outside the Neptunian "Desert" and "Ridge" (A. Castro-González et al. 2024), it is able to securely retain its atmosphere from evaporation (J. E. Owen 2019). TIC 118798035 b was never massive enough to trigger the runaway gas accretion to become a Jovian planet. One possibility is that the core of this planet was formed inefficiently inside the snow line from refractory material. Another possibility is that it was initially formed beyond the snow line (J. Venturini & R. Helled 2017), but the presence of the other two massive planets acted as a barrier for the inward flux of volatile pebbles and/or planetesimals, which prevented the core of TIC 118798035 b from becoming the embryo of a Jovian planet (B. Bitsch & A. Izidoro 2023).

The TIC 118798035 system is a unique target for future exoplanet atmospheric studies. With three transiting exoplanets spanning masses from Jupiter to sub-Neptunes, the system offers an opportunity to test mass–metallicity relationships that have been elusive with other multiplanet systems in the Neptune/sub-Neptune regime alone (see, e.g., J. E. Libby-Roberts et al. 2020; S. Barat et al. 2024). As showcased in Figure 11, the maximum atmospheric metallicities all range between solar and above $\times 10$ solar, implying that well-known atmospheric features such as CO_2 on the more massive planets c and d might be detectable with instrumentation such as that on board JWST (JWST Transiting Exoplanet Community Early Release Science Team et al. 2023). The sub-Neptune-mass planet TIC 11879803 b, on the other hand, falls in an interesting region of parameter space—it orbits a similar star and has very similar bulk properties to (although it is more inflated than) TOI-421 b, which has been recently shown to be a likely haze-free, low-metallicity world (B. Davenport et al. 2025). If TIC 11879803 b has similar atmospheric properties to TOI-421 b, then its atmospheric features should be readily detectable with JWST. Having a stellar brightness comparable to that of WASP-39, the planets in the TIC 11879803 system could be observed with JWST/NIRSpec PRISM with only mild saturation in the 1–2 μm range, enabling detection of the expected H_2O and CO_2 absorption features (Z. Rustamkulov et al. 2023; A. L. Carter et al. 2024). This atmospheric exploration would allow for a test of whether the mass–metallicity relationship observed in the atmospheres of solar system planets also maps to systems elsewhere.

Acknowledgments

R.B. acknowledges support from FONDECYT project 1241963 and ANID—Millennium Science Initiative—ICN12_009. T.T. acknowledges support by the BNSF program "VIHREN-2021" project No. KP-06-DV/5. A.J. acknowledges support from Fondecyt project 1251439. This Letter was based on observations collected at the European Southern Observatory under ESO programs 114.27CV, 114.27CS, and 115.286G.

This Letter also made use of data collected by the TESS mission that are publicly available from the Mikulski Archive for Space Telescopes (MAST), operated by the Space Telescope Science Institute (STScI). Funding for the TESS mission is provided by NASA's Science Mission Directorate. We acknowledge the use of public TESS data from pipelines at the TESS Science Office and the TESS Science Processing Operations Center. Resources supporting this work were provided by the NASA High-End Computing (HEC) program through the NASA Advanced Supercomputing (NAS) division at Ames Research Center for the production of the SPOC data products.

This research has made use of the Exoplanet Follow-up Observation Program (ExoFOP) and NASA Exoplanet

Archive websites, which are operated by the California Institute of Technology under contract with NASA under the Exoplanet Exploration Program.

Based on observations obtained with the HATPI project at the Las Campanas Observatory of the Carnegie Institution for Science. HATPI is operated by the Department of Astrophysical Sciences at Princeton University. External funding for HATPI has been provided by the Gordon and Betty Moore Foundation, the David and Lucile Packard Foundation, the Mount Cuba Astronomical Foundation, and the Agencia Nacional de Investigación y Desarrollo (ANID) of Chile through QUIMAL, Millennium, and Fondecyt grants.

Facilities: VLT:Kueyen, TESS, ESO:3.6m (HARPS), Max Planck:2.2m (FEROS).

Software: `astropy` (Astropy Collaboration et al. 2013, 2018, 2022), `batman` (L. Kreidberg 2015), `ceres` (R. Brahm et al. 2017a), `celerite` (D. Foreman-Mackey et al. 2017), `dynesty` (J. S. Speagle 2020), `exostriker` (T. Trifonov 2019), `juliet` (N. Espinoza et al. 2019), `lightkurve` (Lightkurve Collaboration et al. 2018), `radvel` (B. J. Fulton et al. 2018), `serval` (M. Zechmeister et al. 2018), `zaspe` (R. Brahm et al. 2017b).

Appendix

The posterior probability distributions obtained with our TTV and RV modelling are presented in Figure A1.

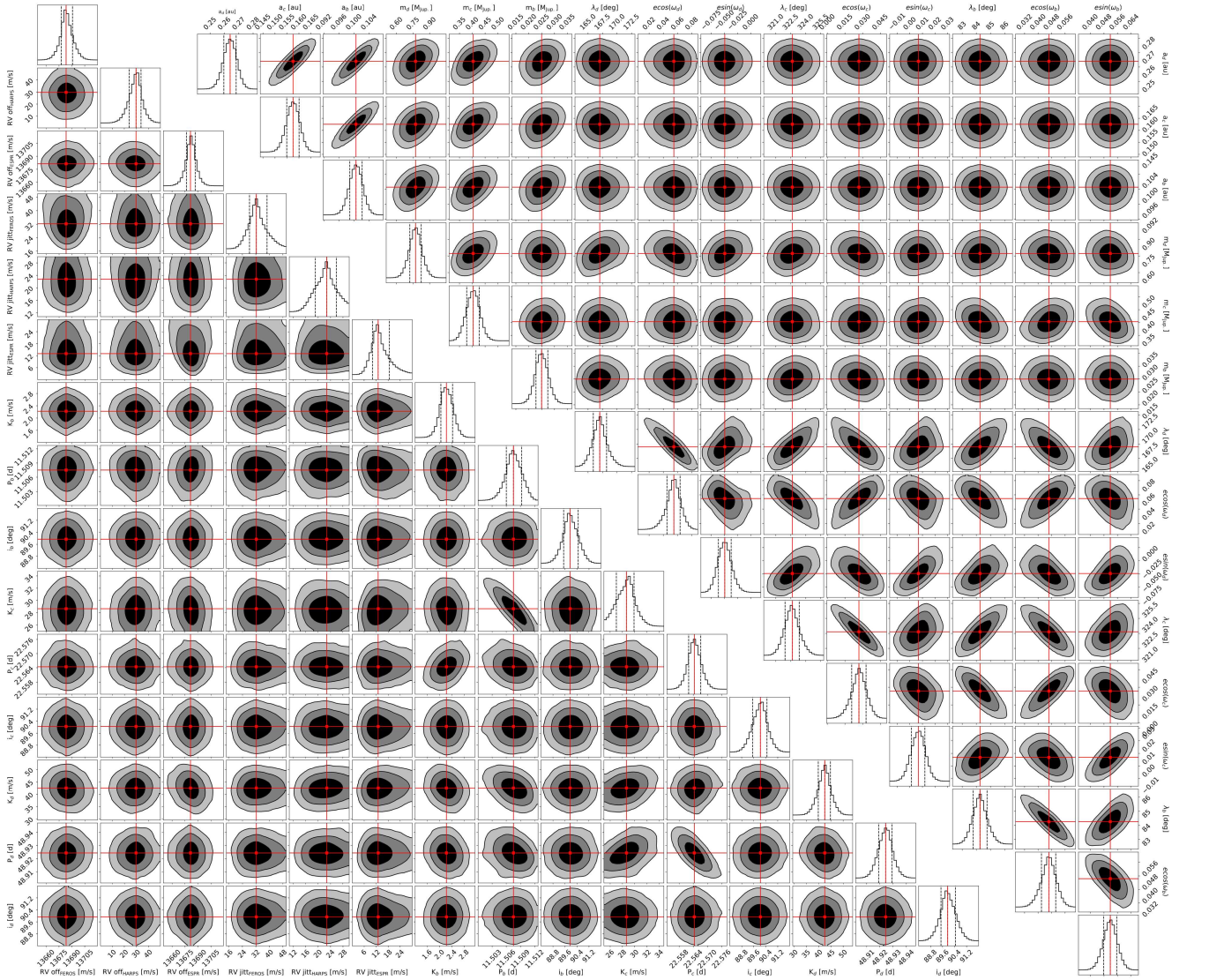

Figure A1. Posterior probability distributions from the joint TTV and RV MCMC modeling of TIC 118798035. The median values of the fitted and derived parameters are indicated by red lines that create the shape of a plus sign. Black contours mark the 1σ, 2σ, and 3σ confidence intervals of the distributions.

ORCID iDs

Rafael Brahm https://orcid.org/0000-0002-9158-7315
Trifon Trifonov https://orcid.org/0000-0002-0236-775X
Andrés Jordán https://orcid.org/0000-0002-5389-3944
Thomas Henning https://orcid.org/0000-0002-1493-300X
Néstor Espinoza https://orcid.org/0000-0001-9513-1449
Felipe I. Rojas https://orcid.org/0000-0003-3047-6272
Marcelo Tala Pinto https://orcid.org/0009-0004-8891-4057
Daniel Thorngren https://orcid.org/0000-0002-5113-8558
Lorena Acuña https://orcid.org/0000-0002-9147-7925
Jan Eberhardt https://orcid.org/0000-0003-3130-2768
Helem Salinas https://orcid.org/0009-0009-8795-4563
Michaela Vítková https://orcid.org/0000-0002-2994-2929
Juan I. Espinoza-Retamal https://orcid.org/0000-0001-9480-8526
Gaspar Bakos https://orcid.org/0000-0001-7204-6727
Attila Bódi https://orcid.org/0000-0002-8585-4544
Gavin Boyle https://orcid.org/0009-0009-2966-7507
Joel Hartman https://orcid.org/0000-0001-8732-6166
Anthony Keyes https://orcid.org/0009-0007-3707-4846
Vincent Suc https://orcid.org/0000-0001-7070-3842
Geert Jan Talens https://orcid.org/0000-0003-4787-2335

References

Acuña, L., Kreidberg, L., Zhai, M., & Mollière, P. 2024, A&A, 688, A60
Astropy Collaboration, Price-Whelan, A. M., Lim, P. L., et al. 2022, ApJ, 935, 167
Astropy Collaboration, Price-Whelan, A. M., Sipőcz, B. M., et al. 2018, AJ, 156, 123
Astropy Collaboration, Robitaille, T. P., Tollerud, E. J., et al. 2013, A&A, 558, A33
Baranne, A., Queloz, D., Mayor, M., et al. 1996, A&AS, 119, 373
Barat, S., Désert, J.-M., Goyal, J. M., et al. 2024, A&A, 692, A198
Bergez-Casalou, C., Bitsch, B., & Raymond, S. N. 2023, A&A, 669, A129
Bitsch, B., & Izidoro, A. 2023, A&A, 674, A178
Bloot, S., Miguel, Y., Bazot, M., & Howard, S. 2023, MNRAS, 523, 6282
Bourrier, V., Attia, M., Mallonn, M., et al. 2023, A&A, 669, A63
Bozhilov, V., Antonova, D., Hobson, M. J., et al. 2023, ApJL, 946, L36
Brahm, R., Espinoza, N., Jordán, A., et al. 2019, AJ, 158, 45
Brahm, R., Jordán, A., & Espinoza, N. 2017a, PASP, 129, 034002
Brahm, R., Jordán, A., Hartman, J., & Bakos, G. 2017b, MNRAS, 467, 971
Brahm, R., Ulmer-Moll, S., Hobson, M. J., et al. 2023, AJ, 165, 227
Brakensiek, J., & Ragozzine, D. 2016, ApJ, 821, 47
Bressan, A., Marigo, P., Girardi, L., et al. 2012, MNRAS, 427, 127
Carter, A. L., May, E. M., Espinoza, N., et al. 2024, NatAs, 8, 1008
Castro-González, A., Bourrier, V., Lillo-Box, J., et al. 2024, A&A, 689, A250
Chabrier, G., & Debras, F. 2021, ApJ, 917, 4
Chachan, Y., Fortney, J. J., Ohno, K., Thorngren, D., & Murray-Clay, R. 2025, ApJ, 994, 43
Danti, C., Bitsch, B., & Mah, J. 2023, A&A, 679, L7
Davenport, B., Kempton, E. M. R., Nixon, M. C., et al. 2025, ApJL, 984, L44
David, T. J., Cody, A. M., Hedges, C. L., et al. 2019, AJ, 158, 79
Dawson, R. I., Huang, C. X., Brahm, R., et al. 2021, AJ, 161, 161
Dawson, R. I., & Johnson, J. A. 2018, ARA&A, 56, 175
Duncan, M. J., Levison, H. F., & Lee, M. H. 1998, AJ, 116, 2067
Eberhardt, J., Trifonov, T., Henning, T., et al. 2025, AJ, 169, 298
Espinoza, N., Kossakowski, D., & Brahm, R. 2019, MNRAS, 490, 2262
Espinoza-Retamal, J. I., Jordán, A., Brahm, R., et al. 2025, AJ, 170, 70
Fabrycky, D. C., Ford, E. B., Steffen, J. H., et al. 2012, ApJ, 750, 114
Finociety, B., Donati, J. F., Cristofari, P. I., et al. 2023, MNRAS, 526, 4627
Foreman-Mackey, D., Agol, E., Angus, R., & Ambikasaran, S. 2017, AJ, 154, 220
Foreman-Mackey, D., Hogg, D. W., Lang, D., & Goodman, J. 2013, PASP, 125, 306
Fortney, J. J., Marley, M. S., & Barnes, J. W. 2007, ApJ, 659, 1661
Fulton, B. J., Petigura, E. A., Blunt, S., & Sinukoff, E. 2018, PASP, 130, 044504
Gaia Collaboration, Vallenari, A., Brown, A. G. A., et al. 2023, A&A, 674, A1
Goldreich, P., & Schlichting, H. E. 2014, AJ, 147, 32
Goldreich, P., & Tremaine, S. 1979, ApJ, 233, 857
Goodman, J., & Weare, J. 2010, CAMCS, 5, 65
Hord, B. J., Colón, K. D., Kostov, V., et al. 2021, AJ, 162, 263
Howard, S., Guillot, T., Bazot, M., et al. 2023, A&A, 672, A33
Howard, S., Helled, R., & Müller, S. 2025, A&A, 693, L7
Huang, C., Wu, Y., & Triaud, A. H. M. J. 2016, ApJ, 825, 98
Jordán, A., Brahm, R., Espinoza, N., et al. 2020, AJ, 159, 145
JWST Transiting Exoplanet Community Early Release Science Team, Ahrer, E.-M., Alderson, L., et al. 2023, Natur, 614, 649
Kaufer, A., Stahl, O., Tubbesing, S., et al. 1999, Msngr, 95, 8
Kreidberg, L. 2015, PASP, 127, 1161
Leconte, J., & Chabrier, G. 2012, A&A, 540, A20
Lee, M., & Peale, S. 2003, ApJ, 592, 1201
Libby-Roberts, J. E., Berta-Thompson, Z. K., Désert, J.-M., et al. 2020, AJ, 159, 57
Lightkurve Collaboration, Cardoso, J. V. D. M., Hedges, C., et al., 2018 Lightkurve: Kepler and TESS Time Series Analysis in Python, Astrophysics Source Code Library, ascl:1812.013
Masuda, K., Libby-Roberts, J. E., Livingston, J. H., et al. 2024, AJ, 168, 294
Miguel, Y., Guillot, T., & Fayon, L. 2016, A&A, 596, A114
Militzer, B., & Hubbard, W. B. 2013, ApJ, 774, 148
Militzer, B., Wahl, S., & Hubbard, W. B. 2019, ApJ, 879, 78
Munari, U., Henden, A., Frigo, A., et al. 2014, AJ, 148, 81
Nelder, J. A., & Mead, R. 1965, CompJ, 7, 308
Owen, J. E. 2019, AREPS, 47, 67
Pepe, F., Cristiani, S., Rebolo, R., et al. 2021, A&A, 645, A96
Pepe, F., Mayor, M., Rupprecht, G., et al. 2002, Msngr, 110, 9
Petrovich, C. 2015, ApJ, 799, 27
Podolak, M., Helled, R., & Schubert, G. 2019, MNRAS, 487, 2653
Pollack, J. B., Hubickyj, O., Bodenheimer, P., et al. 1996, Icar, 124, 62
Ragozzine, D., & Holman, M. J. 2010, arXiv:1006.3727
Rice, M., Wang, S., Wang, X.-Y., et al. 2022, AJ, 164, 104
Ricker, G. R., Winn, J. N., Vanderspek, R., et al. 2015, JATIS, 1, 014003
Rustamkulov, Z., Sing, D. K., Mukherjee, S., et al. 2023, Natur, 614, 659
Salinas, H., Brahm, R., Olmschenk, G., et al. 2025, MNRAS, 538, 2031
Schneider, A. D., & Bitsch, B. 2021, A&A, 654, A71
Shaw, D. E., Weiss, L. M., Agol, E., et al. 2025, AJ, 170, 146
Shibata, S., Helled, R., & Ikoma, M. 2020, A&A, 633, A33
Skrutskie, M. F., Cutri, R. M., Stiening, R., et al. 2006, AJ, 131, 1163
Speagle, J. S. 2020, MNRAS, 493, 3132
Stassun, K. G., Oelkers, R. J., Paegert, M., et al. 2019, AJ, 158, 138
Stassun, K. G., Oelkers, R. J., Pepper, J., et al. 2018, AJ, 156, 102
Tan, X., Payne, M. J., Lee, M. H., et al. 2013, ApJ, 777, 101
Tayar, J., Claytor, Z. R., Huber, D., & van Saders, J. 2022, ApJ, 927, 31
TESS Team 2022, TESS Calibrated Full Frame Images: All Sectors, STScI/MAST,
Thompson, S. L. 1990, ANEOS Analytic Equations of State for Shock Physics Codes Input Manual,
Thorngren, D., & Fortney, J. J. 2019, ApJL, 874, L31
Thorngren, D. P., Fortney, J. J., Murray-Clay, R. A., & Lopez, E. D. 2016, ApJ, 831, 64
Trifonov, T., 2019 The Exo-Striker: Astrophysics Source Code Library, ascl:1906.004
Trifonov, T., Brahm, R., Espinoza, N., et al. 2021, AJ, 162, 283
Trifonov, T., Brahm, R., Jordán, A., et al. 2023, AJ, 165, 179
Trifonov, T., Kürster, M., Zechmeister, M., et al. 2017, A&A, 602, L8
Venturini, J., & Helled, R. 2017, ApJ, 848, 95
Vítková, M., Brahm, R., Trifonov, T., et al. 2025, ApJL, 978, L22
Winn, J. N., & Fabrycky, D. C. 2015, ARA&A, 53, 409
Zechmeister, M., Reiners, A., Amado, P. J., et al. 2018, A&A, 609, A12